IEEE Access
Multidisciplinary ⋮ Rapid Review ⋮ Open Access Journal

Received November 4, 2021, accepted December 16, 2021, date of publication December 23, 2021, date of current version January 11, 2022.

Digital Object Identifier 10.1109/ACCESS.2021.3138274

DC Bus Voltage Control of Wind Power Inverter Based on First-Order LADRC

CHANGSHENG YUAN[1,2], XUESONG ZHOU[2], AND YOUJIE MA[2]
[1]The 16th Research Institute of China Electronics Technology Group Corporation, Hefei 230093, China
[2]Tianjin Key Laboratory for Control Theory and Applications in Complicated Industry Systems, School of Electrical and Electronic Engineering, Tianjin University of Technology, Tianjin 300384, China

Corresponding author: Changsheng Yuan (eeycs1806@163.com)

This work was supported in part by the National Natural Science Foundation of China under Grant 51877152, and in part by the Tianjin Natural Science Foundation under Grant 18jczdjc97300.

ABSTRACT The wind power grid-connected inverter system has the characteristics of non-linearity, strong coupling, and susceptibility to grid voltage fluctuations and non-linear loads. To obtain the ideal control effect, the improved linear active disturbance rejection controller (LADRC) controls the voltage outer loop. Firstly, the mathematical model of the wind power grid-connected inverter is analyzed, on this basis, a linear active disturbance rejection control based on the reduced-order linear extended state observer is designed, reduce the phase lag of the observer, improve the system's disturbance observation accuracy; reference lead correction lag correction method, the observer gain is improved and connected in series to the total disturbance channel to reduce the noise amplification effect of the observer; through frequency domain response characteristic analysis, the results show that the improved LADRC has better disturbance rejection performance. The simulation results of various working conditions show that the improved method has better rapidity and immunity compared with traditional LADRC.

INDEX TERMS Grid inverter, linear active disturbance rejection control, linear extended state observer, lead and lag link, frequency domain analysis.

I. INTRODUCTION

With the rapid development and successful application of high-power power electronic devices, direct-drive permanent magnet wind power generation system has become one of the main models of wind power generation in China [1], [2], the direct-drive permanent magnet wind generator set realizes the isolation between the generator and the large power grid through the back-to-back dual pulse width modulation converter. However, due to the randomness and intermittent nature of wind power generation, improving the control strategy of wind power grid-connected inverters and grid-connected power quality is still a current research hotspot. Grid-connected inverters are an important part of energy conversion in wind power generation systems, the disturbance is mainly composed of two parts: Disturbance caused by changes in the internal parameters of the converter and changes in external conditions [3], [4]. Generally, the DC side capacitance can be increased to suppress the fluctuation of DC bus voltage, but this will reduce the response speed of the system, increase the cost of power generation and reduce reliability. Therefore, the research and application of grid-connected inverter control strategies have great engineering significance.

The current control methods of grid-connected inverters mainly include voltage-oriented control, direct power control, and nonlinear control [5], [6]. Reference [7] analyzes the grid side inverter control strategy based on grid voltage vector orientation, the unit factor grid connection of the system is realized, the effectiveness of the control strategy is verified by simulation. Reference [8] proposed to replace the traditional PI controller with fuzzy PI control technology and neural network PI control technology, improve the sine fullness of the grid-connected current, reduce harmonic content. References [9], [10] uses synovial variable structure control in the outer voltage loop, the inner loop adopts predictive current control, the harmonic current at the grid side is effectively suppressed, making the DC side voltage more stable. However, the above studies have ignored the influence of changes in the external environment, system model

The associate editor coordinating the review of this manuscript and approving it for publication was Nishant Unnikrishnan.

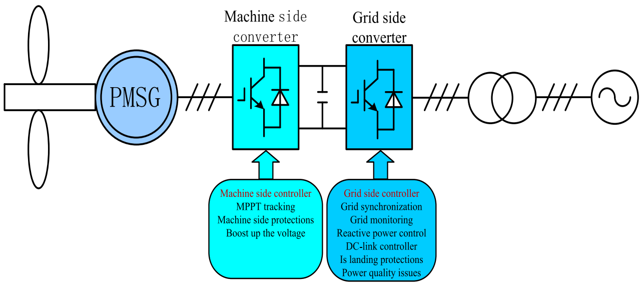

FIGURE 1. Schematic diagram of permanent magnet wind power generation system.

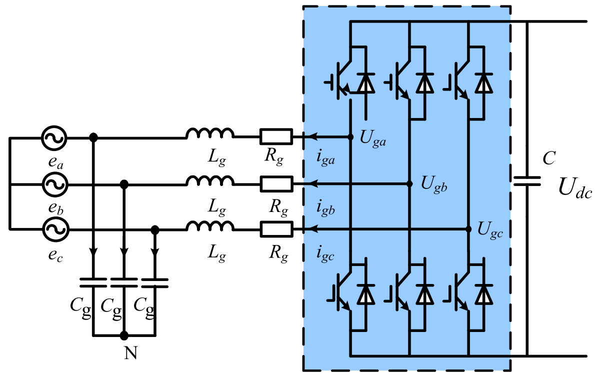

FIGURE 2. Overall control block diagram of wind power inverter.

uncertainty, and internal parameter perturbation on the DC side voltage, in severe cases, the stability of the system will be affected.

At present, active disturbance rejection control has made great progress in many fields, for example, precision control, motor speed control system and other fields, it has become a strong competitor of the traditional PID control method. In reference [11], nonlinear ADRC has been applied to inverter, however, the controller design is complex and has many parameters; in reference [12], by introducing the differential term of output voltage error, increased LESO's observer bandwidth, however, the parameters of LESO after the transformation has doubled, making it difficult to set; reference [13] deleted the known outputs in the system from the linear extended state observer, proposed the LADRC of the reduced-order linear extended state observer (RLESO), the phase lag of the system is reduced to a certain extent, the immunity and robustness of LADRC are improved.

In this paper, the DC bus voltage is taken as the control object, a linear active disturbance rejection control is constructed to replace the voltage outer loop control. Since the DC bus voltage can be accurately obtained in real-time through the measurement link, remove it from LESO, a reduced-order LESO is constructed that takes the differential of the DC bus voltage and the error of its observed value as the feedback quantity. Refer to the idea of leading correction and lag correction, make corresponding improvements to the observer gain and connect its correction link in series to the total disturbance channel, reducing its noise amplification effect. The frequency-domain analysis proves that the anti-interference performance of the improved LADRC is better than that of the traditional LADRC, the effectiveness of the strategy proposed in this paper is verified by simulation.

II. MATHEMATICAL MODEL AND CONTROL STRATEGY OF GRID CONNECTED INVERTER

Figure 1 is a schematic diagram of a direct-drive permanent magnet wind power generation system, the random wind speed causes the generator to output a constantly changing current, it is converted into DC with constant voltage through the rectifier at the machine side, through the intermediate DC voltage stabilizing link, the electric energy is fed into the power grid by the grid side inverter. By controlling the generator-side converter to control the output active power of the generator, and then achieve the capture of the maximum wind energy of the generator, to realize the decoupling of output active power and reactive power, the control network side converter [14], [15].

Fig. 2 is the control block diagram of grid side inverter of wind power generation, R_g is the equivalent resistance on the grid side, L_g is the inductance of the grid-side filter, e_a, e_b and e_c are output voltages respectively, C_g is the grid side filter capacitor, C is the bus filter capacitor, U_{dc} is the DC bus voltage.

According to the topology of grid side inverter, KVL three-phase voltage equation is obtained as follows:

$$\begin{bmatrix} U_{ga} \\ U_{gb} \\ U_{gc} \end{bmatrix} = \begin{bmatrix} e_a \\ e_b \\ e_c \end{bmatrix} + R_g \begin{bmatrix} i_{ga} \\ i_{gb} \\ i_{gc} \end{bmatrix} + L_g \frac{d}{dt} \begin{bmatrix} i_{ga} \\ i_{gb} \\ i_{gc} \end{bmatrix} \tag{1}$$

$$\begin{bmatrix} i_{ga} \\ i_{gb} \\ i_{gc} \end{bmatrix} = \begin{bmatrix} i_a \\ i_b \\ i_c \end{bmatrix} + C_g \frac{d}{dt} \begin{bmatrix} U_{Ca} \\ u_{Cb} \\ u_{Cc} \end{bmatrix} \tag{2}$$

where: U_{ga}, U_{gb}, U_{gc} are the voltages of the three-phase grid-side inverter; i_{ga}, i_{gb}, i_{gc} are the three-phase grid-side inverter currents respectively.

After coordinate transformation [16], it can be known that:

$$\begin{bmatrix} U_{gd} \\ U_{gq} \end{bmatrix} = \begin{bmatrix} e_d \\ e_q \end{bmatrix} + R_g \begin{bmatrix} i_{gd} \\ i_{gq} \end{bmatrix} + L_g \frac{d}{dt} \begin{bmatrix} i_{gd} \\ i_{gq} \end{bmatrix} + L_g \begin{bmatrix} -wi_{gq} \\ wi_{gd} \end{bmatrix} \tag{3}$$

$$\begin{bmatrix} i_{gd} \\ i_{gq} \end{bmatrix} = \begin{bmatrix} i_d \\ i_q \end{bmatrix} + C_g \frac{d}{dt} \begin{bmatrix} e_d \\ e_q \end{bmatrix} + \begin{bmatrix} -we_q \\ we_d \end{bmatrix} \tag{4}$$

where: U_{gd} and U_{gq} are the d and q axis components of the grid-side inverter voltage respectively; e_d and e_q are the d and q axis components of the three-phase grid voltage respectively; i_{gd} and i_{gq} are the d and q axis components of the three-phase grid-side inverter current respectively; i_d and i_q are the components of the output current on the d and q axes; w is the angular frequency of the grid output by the phase-locked loop.

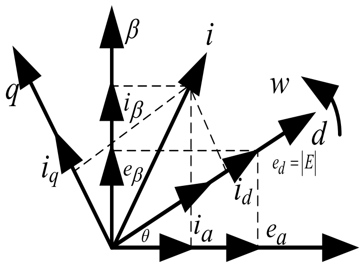

FIGURE 3. The grid-side voltage and current vector diagrams in α-β and d-q coordinate systems.

Derivation and simplification of (3) formula, and substituting formula (2) into it can be obtained:

$$\frac{d^2}{dt^2}\begin{bmatrix} e_d \\ e_q \end{bmatrix} = \frac{1}{C_g L_g}\begin{bmatrix} U_{gd} \\ U_{gq} \end{bmatrix} - \frac{1}{C_g L_g}\begin{bmatrix} e_d \\ e_q \end{bmatrix} - \frac{R_g}{C_g L_g}\begin{bmatrix} i_{gd} \\ i_{gq} \end{bmatrix} + \frac{1}{C_g}\begin{bmatrix} wi_{gq} \\ -wi_{gd} \end{bmatrix} - \frac{d}{C_g dt}\begin{bmatrix} i_d \\ i_q \end{bmatrix} + \frac{d}{C_g dt}\begin{bmatrix} we_q \\ -we_d \end{bmatrix} \tag{5}$$

According to equation (5), the wind power grid side inverter is a multivariable and highly coupled system, therefore, the application of traditional control strategies cannot well meet the control standards required by the industry.

The voltage-oriented vector control of grid-connected inverter generally adopts the double PI control structure of voltage outer loop and current inner loop [6]. Under this control mode, the stability of DC side voltage can be maintained, and it can make the AC side output a good sinusoidal current waveform, making the inverter meet the requirements of unity power factor grid connection. The control of the voltage outer loop is adjusted based on the difference between the given DC side voltage and the feedback, to achieve the purpose of maintaining voltage stability, the output of the outer loop is given as the d-axis current of the inner loop, the current inner loop is mainly to achieve fast-tracking of the given.

During the coordinate transformation process, align the d-axis direction with the grid voltage space vector E, that is, the peak point of phase a of the grid voltage is taken as the zero point of the rotation angle θ, at this time, there are vector diagrams in $e_d = |E|$, $e_q = 0$, $\alpha - \beta$ and $d - q$ coordinate systems as shown in Figure 3 [6].

In Figure 3, i_d and i_q are the active and reactive components in the side currents respectively; u_d, u_q are the output control quantities. In the steady-state, since i_d and i_q are both direct current, their differential term is equal to zero, according to formula (3), we can get:

$$\begin{cases} U_d = e_d - R_g i_d + wLi_q \\ U_q = -R_g i_q - wLi_d \end{cases} \tag{6}$$

In the double closed-loop structure, to maintain the stability of the DC bus voltage, regard the output of the voltage outer loop as the given value of the active current of the current inner loop; the reactive current is given externally, to realize unity power factor grid connection, the given value

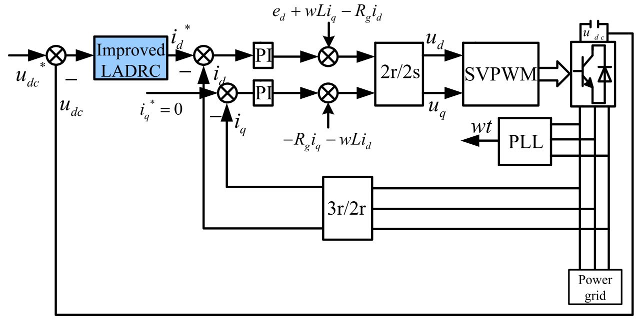

FIGURE 4. Grid side inverter grid voltage vector directional control block diagram.

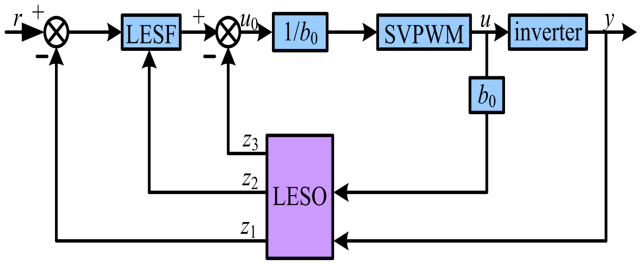

FIGURE 5. The overall structure of LADRC.

of reactive current is set to zero [17]. After the active and reactive currents are fed back through the current inner loop, the closed-loop output is superimposed on the steady-state control equation to output the control variables u_d, u_q. It can be seen from the figure below that after ud and uq are output as the control quantity, will be connected to the space vector pulse width modulation strategy interface, controlling the turn-on and turn-off of the grid-side inverter. Figure 4 is a block diagram of grid-side inverter voltage-oriented vector control.

III. STRUCTURAL DESIGN OF LINEAR ACTIVE DISTURBANCE REJECTION CONTROLLER

Traditional LADRC is composed of three parts: linear state error feedback rate (LSEF), linear extended state observer (LESO), and linear tracking differentiator (LTD), as shown in Figure 5; the role of LTD is to arrange the transition process, eliminate the contradiction between overshoot and rapidity [18], extract the differential signal, to avoid the high-frequency oscillation of the bus voltage, this article does not use LTD; in Figure 5, v is the DC bus voltage reference value, b_0 is the control gain, u is the control quantity, the physical meaning is the inverter output voltage, z_1, z_2, z_3 are the system output and its differential and total disturbance observed by LESO, and y is the output of the system.

A. LADRC STRUCTURE DESIGN BASED ON RLESO

From equation (5), it can be known that the controlled object is a second-order system, and its expression is

$$\ddot{y} = f(y, \dot{y}, w, t) + bu = -a_1\dot{y} - a_0 y + w + bu \tag{7}$$

In the formula, y and u are output and input respectively, and w is a disturbance. a_1, a_0, and w are all unknown, part b is known (the known part is denoted as b_0), then the above formula can be written as:

$$\ddot{y} = -a_1\dot{y} - a_0 y + w + (b - b_0)u + b_0 u = f + b_0 u \quad (8)$$

Among them, $f = -a_1\dot{y} - a_0 y + w + (b - b_0)u$ is the total disturbance including external disturbance and internal disturbance.

Select state variables: $x_1 = y$, $x_2 = \dot{y}$, $x_3 = f$, then transform the above equation into a continuous expanded state space description:

$$\begin{cases} \begin{bmatrix} \dot{x}_1 \\ \dot{x}_2 \\ \dot{x}_3 \end{bmatrix} = \begin{bmatrix} 0 & 1 & 0 \\ 0 & 0 & 1 \\ 0 & 0 & 0 \end{bmatrix} \begin{bmatrix} x_1 \\ x_2 \\ x_3 \end{bmatrix} + \begin{bmatrix} 0 & 0 \\ b_0 & 0 \\ 0 & 1 \end{bmatrix} \begin{bmatrix} u \\ h \end{bmatrix} \\ y = x_1 \end{cases} \quad (9)$$

The third-order continuous linear extended state observer corresponding to the above equation is:

$$\begin{cases} \dot{z}_1 = z_2 - \beta_1 (z_1 - y) \\ \dot{z}_2 = z_3 + b_0 u - \beta_2 (z_1 - y) \\ \dot{z}_3 = -\beta_3 (z_1 - y) \end{cases} \quad (10)$$

where z_1, z_2, and z_3 are the observed values of DC bus voltage, DC bus voltage differential and total disturbance respectively, β_1, β_2, and β_3 are the observer gains. Because the DC bus voltage (y) can be observed at any time, then the corresponding related structure can be deleted in formula (10), and the difference between the differential $\dot{f}$ of the DC bus voltage and the corresponding state estimated by the observer is used as feedback to be corrected, Thus, the second-order linear extended state observer (RLESO) equation is obtained:

$$\begin{cases} \dot{z}_1 = z_2 + b_0 u - \beta_1 (z_1 - \dot{y}) \\ \dot{z}_2 = -\beta_2 (z_1 - \dot{y}) \end{cases} \quad (11)$$

In the formula, z_1 is the observation value of $\dot{f}$, and z_2 is the observation value of f. Choose the appropriate observer gain, the observer will be able to realize real-time tracking of the DC bus voltage differential and total disturbance.

RLESO's disturbance compensation and LSEF are designed as:

$$u = \frac{K_p(r - y) - K_d z_1 - z_2}{b_0} \quad (12)$$

In the formula, K_p and K_d are the controller parameters, and r is the set value of the controller. At this time, if the observation error of z_2 to f is ignored, the system (8) can be simplified to an integral series structure. According to formula (12), the closed-loop transfer function of the system can be obtained as:

$$G(s) = \frac{Y(s)}{R(s)} = \frac{K_p}{s^2 + 2K_d s + K_p} \quad (13)$$

According to the pole configuration method [19], the RLESO in equations (11) and (12) are configured as follows:

$$\beta = \begin{bmatrix} \beta_1 & \beta_2 \end{bmatrix} = \begin{bmatrix} 2w_0 & w_0^2 \end{bmatrix} \quad (14)$$

$$K = \begin{bmatrix} k_p & k_d \end{bmatrix} = \begin{bmatrix} w_c^2 & 2w_c \end{bmatrix} \quad (15)$$

where: w_0 is the bandwidth of the observer; w_c is the bandwidth of the controller; in this way, the LADRC control parameter configuration problem can be simplified to the design of the observer bandwidth w_0 and the observer bandwidth w_c.

B. IMPROVED LADRC STRUCTURE DESIGN

LESO is the core of LADRC technology, and its disturbance estimation capability is the key to affecting LADRC performance. Next, based on the analysis of the original RLESO, combined with the specific characteristics of the control object, design and improve RLESO.

1) RLESO CHARACTERISTIC ANALYSIS

According to formulas (11) and (14), the transfer functions of z_1 and z_2 can be obtained as

$$z_1 = \frac{2w_o s^2 + w_o^2 s}{(s + w_0)^2} y + \frac{b_0 s}{(s + w_0)^2} u \quad (16)$$

$$z_2 = \frac{w_0^2 s^2}{(s + w_0)^2} y - \frac{w_0^2 b_0}{(s + w_0)^2} u \quad (17)$$

Literature [20] proposed that in order to speed up the tracking speed of RLESO, the observer bandwidth should be increased, at the same time, from both the time domain and frequency domain, demonstrated the error observation and filtering performance of the second-order RLESO, mainly focus on stability and anti-interference performance, but did not analyze its rapidity, that is, the dynamic observation performance of RLESO, the tracking effect of the total disturbance directly affects the transient effect of the system output, which will be analyzed below.

From equation (8)

$$f = \ddot{y} - b_0 u \quad (18)$$

Combining equations (16) and (17), the disturbance observation transfer function of RLESO can be obtained as

$$G_1(s) = \frac{z_2}{f} = \frac{w_o^2}{(s + w_0)^2} \quad (19)$$

Figure 6 shows the comparison of disturbance observation capabilities between traditional LESO and RLESO. It can be seen from the figure that the bandwidth of RLESO increases, which improves the disturbance observation ability of LESO, at the same time, the phase lag of RLESO is reduced, and the response speed of the observer is accelerated. However, the attenuation degree of its high-frequency band is reduced, and it is susceptible to the influence of high-frequency noise.

2) IMPROVED RLESO DESIGN

Although RLESO has improved the disturbance observation ability of the observer to a certain extent, reducing the phase lag degree of disturbance observation, but also increase its noise amplification phenomenon. Therefore, referring to the idea of super front correction and lag correction in classical

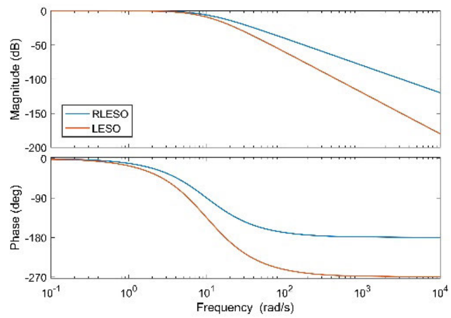

FIGURE 6. Comparison of disturbance observation capabilities between traditional LESO and RLESO.

control theory, the observer parameters are improved and a lead-lag correction link is added to the total disturbance channel.

Comparing the above formula (19) with a typical second-order system, we can see that

$$\begin{cases} w_n = \sqrt{\beta_2} \\ \zeta = \dfrac{\beta_1}{2\sqrt{\beta_2}} \end{cases} \tag{20}$$

In formula (20), w_n is the angular frequency of the standard second-order system, ζ is the damping ratio. In the second-order system, w_n and ζ determine the time and frequency response, among them, β_2 has the greatest impact on w_n and ζ. Therefore, the observer gain coefficient β_2 is improved.

Refer to the method of leading correction and lag correction, the improvements are as follows

$$\hat{\beta}_2 = \beta_2 \frac{T_a s + 1}{\alpha T_a s + 1} \tag{21}$$

In formula (21), T_a is the leading time constant; α is a coefficient between 0 and 1, then the disturbance observation transfer function of the new RLESO is:

$$G_2(s) = \frac{\hat{\beta}_2 T_a s + \hat{\beta}_2}{a T_a s^3 + (a T_a \beta_1 + 1)s^2 + (\beta_1 + \hat{\beta}_2 T_a)s + \hat{\beta}_2} \tag{22}$$

Compared with equation (22), equation (19) has one more zero point in the left half-plane, the root locus of the system is shifted to the left, which enhances the steady-state and dynamic characteristics of the system.

By introducing the lead-lag link into the total disturbance channel, the dynamic observation ability can be further strengthened, and the disturbance observation ability can be improved, the improved RLESO disturbance observation transfer function is:

$$G_3(s) = \frac{\hat{\beta}_2 T_a s + \hat{\beta}_2}{a T_a s^3 + (a T_a \beta_1 + 1)s^2 + (\beta_1 + \hat{\beta}_2 T_a)s + \hat{\beta}_2} \cdot \frac{T_a s + 1}{\alpha T_a s + 1} \tag{23}$$

Figure 7 above shows the amplitude-frequency characteristic curves of three RLESO disturbance transfer functions.

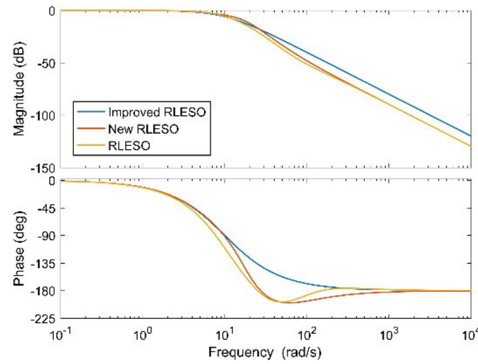

FIGURE 7. Amplitude frequency characteristic curves of three RLESO disturbance transfer functions.

It can be seen that, compared with the aforementioned new RLESO, the improved RLESO has a significant increase in bandwidth and the phase lag in the mid-band is alleviated.

The disturbance compensation and lsef design of the improved RLESO are

$$u = \frac{K_p(r - z_1) - z_3}{b_0} \tag{24}$$

Based on the above analysis, the improved rleso state space is

$$\begin{bmatrix} \dot{z}_1 \\ \dot{z}_2 \\ \dot{z}_3 \end{bmatrix} = \begin{bmatrix} -\beta_1 & 1 & 0 \\ \beta_1 \hat{\beta}_2 T_a - \hat{\beta}_2 & -\hat{\beta}_2 T_a & 0 \\ \dfrac{\beta_1 \hat{\beta}_2 T_a - \hat{\beta}_2}{a} & \dfrac{1}{a T_a} & -\dfrac{1}{a T_a} \end{bmatrix} \begin{bmatrix} z_1 \\ z_2 \\ z_3 \end{bmatrix} + \begin{bmatrix} b_0 & \beta_1 & 0 \\ -\hat{\beta}_2 T_a b_0 & \hat{\beta}_2 - \beta_1 \hat{\beta}_2 T_a & \hat{\beta}_2 T_a \\ 0 & \dfrac{\hat{\beta}_2 - \beta_1 \hat{\beta}_2 T_a}{a} & \dfrac{\hat{\beta}_2 T_a}{a} \end{bmatrix} \begin{bmatrix} u \\ y \\ \dot{y} \end{bmatrix} \tag{25}$$

In the formula: z_3 is the total disturbance finally acting on the system, which is obtained by z_2 through the low-pass filtering link.

Synthesizing formula (12) and formula (25), the structure diagram of the improved LADRC control system can be obtained as shown below.

IV. CONVERGENCE AND FILTERING PERFORMANCE ANALYSIS OF IMPROVED RLESO

The extended state observer is the core of the active disturbance rejection control technology, its tracking and estimation ability is the key to affecting the performance of active disturbance rejection control, therefore, this section first analyzes it.

A. IMPROVED RLESO CONVERGENCE AND ESTIMATION ERROR ANALYSIS

According to formulas (11), (14), (21), the transfer functions of z_1, z_2, and z_3 can be obtained as:

$$z_1 = \frac{2w_0 s + w_0^2}{s^2 + (2w_0 + w_0^2 T_a)s + w_0^2} y$$

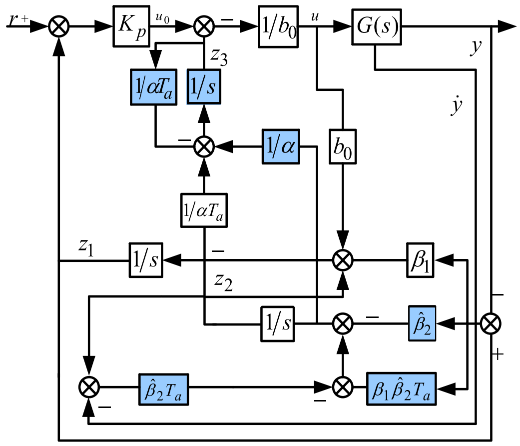

FIGURE 8. Improve the structure of LADRC control system.

$$+\frac{s}{s^2+(2w_0+w_0^2T_a)s+w_0^2}b_0u \tag{26}$$

$$z_2=\frac{w_0^2s-2w_0^3T_as}{s^2+(2w_0+w_0^2T_a)s+w_0^2}y-\frac{w_0^2T_as+w_0^2}{s^2+(2w_0+w_0^2T_a)s+w_0^2}b_0u \tag{27}$$

$$z_3=\frac{T_as+1}{aT_as+1}z_2 \tag{28}$$

Let the tracking error $e_1=z_1-y$, $e_2=z_3-f$, we can get

$$e_1=-\frac{s^2+w_0^2T_as}{s^2+(2w_0+w_0^2T_a)s+w_0^2}y+\frac{s}{s^2+(2w_0+w_0^2T_a)s+w_0^2}b_0u \tag{29}$$

$$e_2=\frac{(w_0^2s-2w_0^3T_as)y-(w_0^2T_as+w_0^2)b_0u}{s^2+(2w_0+w_0^2T_a)s+w_0^2}\times\frac{T_as+1}{aT_as+1}-(s^2y-b_0u) \tag{30}$$

Due to the typicality of the analysis system response, the signal taken by y, u is a step signal whose amplitude is K, Let it be $y(s)=K/s$, $u(s)=K/s$, then the steady-state error is:

$$\begin{cases} e_{1s}=\lim\limits_{s\to 0}se_1=0 \\ e_{2s}=\lim\limits_{s\to 0}se_2=0 \end{cases} \tag{31}$$

The above formula shows that the improved RLESO has the following characteristics and has good performance in convergence and error estimation, and it can complete the error-free estimation of the internal and external disturbances of the system and the internal characteristic variables of the system, it can complete the estimation of system state variables and generalized disturbances without errors.

B. ANALYSIS OF BAND CHARACTERISTICS AND FILTERING PERFORMANCE OF IMPROVED RLESO

Here we focus on the influence of the noise δ_0 of the observation y and the disturbance δ_C of the input end of the

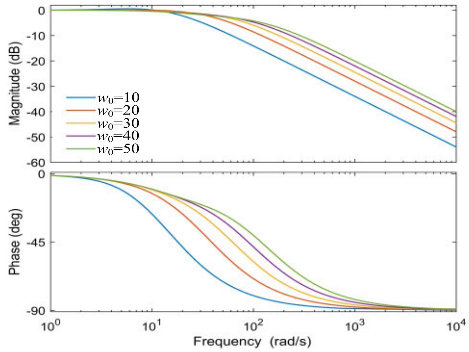

FIGURE 9. Frequency domain characteristic curve of observation noise.

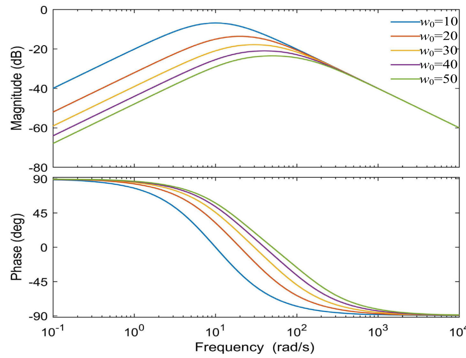

FIGURE 10. Frequency domain characteristic curve of input disturbance.

control quantity u on the improvement of RLESO, according to equation (26), the transfer function of the observed noise δ_0 is:

$$\frac{z_1}{\delta_0}=\frac{2w_0s+w_0^2}{s^2+(2w_0+w_0^2T_a)s+w_0^2} \tag{32}$$

Let $w_0=10, 20, 30, 40, 50$, and get the frequency domain characteristic curve of this function, as shown in Figure 9. The analysis shows that with the increase of w_0, the follow-up response speed of the system increases, but at the same time the high-frequency gain increases, resulting in more pronounced noise amplification.

The transfer function of disturbance δ_c at the input can also be obtained:

$$\frac{z_1}{\delta_c}=\frac{b_0s}{s^2+(2w_0+w_0^2T_a)s+w_0^2} \tag{33}$$

Let $b_0=10$, $w_0=10, 20, 30, 40, 50$, and get the frequency domain characteristics of this transfer function:

Compared with Figure 9, the increase of the observer bandwidth w_0 in Figure 10 can reduce the phase lag of the system tracking input, but the high-frequency band gain is unchanged, it can be seen that the improved RLESO has a strong ability to suppress the disturbance δ_c at the input.

From the above analysis, it can be seen that when subject to observation disturbances and input disturbances, the improved RLESO with the lead-lag link is still effective and robust.

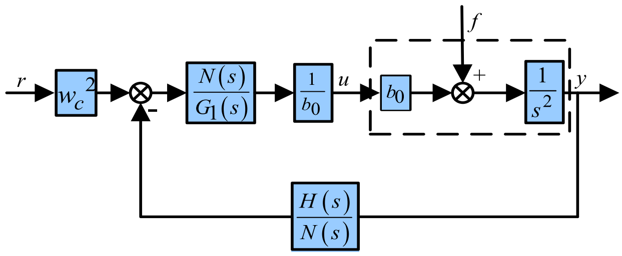

FIGURE 11. Improve the simplified system structure of LADRC.

V. IMMUNITY AND STABILITY ANALYSIS OF IMPROVED LADRC

Previously, the frequency band characteristics and noise suppression ability of improved RLESO were analyzed, This section discusses and analyzes the improvement of the actual system anti-interference performance of LADRC control on this basis.

A. CLOSED LOOP TRANSFER FUNCTION OF IMPROVED LADRC FOR SECOND ORDER OBJECTS

Combining (11), (24) and (28), we can get:

$$u = \frac{1}{b_0}[w_c^2(r - z_1) - z_3] \tag{34}$$

Substituting into equations (26) and (28), we can get

$$u = \frac{N(s)}{G_1(s)\, b_0}(w_c^2 r - \frac{H(s)}{N(s)}y) \tag{35}$$

In formula (32)

$$\begin{aligned} N(s) &= aT_a s^3 + [aT_a(T_a w_0^2 + 2w_0) + 1]s^2 \\ &\quad + (T_a w_0^2 + aT_a w_0^2 + 2w_0)s + w_0^2 \\ G_1(s) &= aT_a s^3 + [aT_a - T_a^2 w_0^2 + aT_a(T_a w_0^2 + 2w_0) + 1]s^2 \\ &\quad + (2w_0 + aT_a w_0^2)s - (T_a w_0^2 - 1)s \\ H(s) &= T_a(w_0^2 - 2T_a w_0^3 + 2w_0 w_c^2)s^2 \\ &\quad + (T_a w_0^2 w_c^2 - 2T_a w_0^3 + 2w_0 w_c^2)s w_0^2 s + w_0^2 w_c^2 \end{aligned}$$

According to formula (18), the accused object can be recorded as

$$y = \frac{1}{s^2}(f + b_0 u) \tag{36}$$

From equations (35) and (36), the structure diagram of the improved LADRC control system is simplified as follows:

From the above-simplified system structure diagram, the closed-loop transfer function of the system can be obtained

$$y = \frac{w_c^2}{(s + w_c)^2} r + \frac{G_1(s)}{s^2 G_1(s) + H(s)} f \tag{37}$$

According to the above equation (37), the tracking term and disturbance term constitute the output of the system. According to the analysis of literature [21], the closed-loop transfer function of the system in the above formula (37) and literature [21] differs only in the disturbance term, indicating that the improved LADRC improves the total disturbance observation ability of the system.

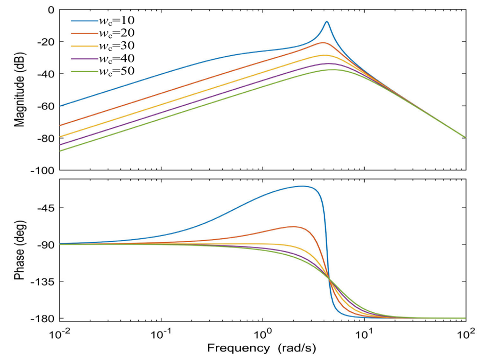

FIGURE 12. Frequency domain characteristic curve of disturbance term (w_c change).

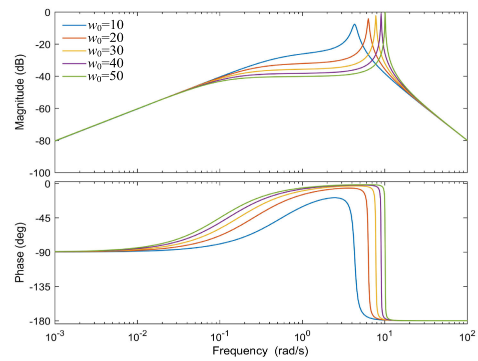

FIGURE 13. Frequency domain characteristic curve of disturbance term (w_0 changes).

B. IMPROVED LADRC ANTI-INTERFERENCE PERFORMANCE ANALYSIS

It can be seen from equation (37) that the disturbance term is related to the controller bandwidth w_c, the observer bandwidth w_0 and the time constant T_a. Let $w_0 = 10$, $T_a = 10$, $w_c = 10$, 20, 30, 40 and 50 to obtain the disturbance amplitude-frequency characteristic curve, as shown in Figure. 12; let $w_c = 10$, $T_a = 10$, $w_0 = 10$, 20, 30, 40, 50 to obtain the disturbance amplitude-frequency characteristic curve, as shown in Figure 13; let $w_c = 10$, $w_0 = 10$, $T_a = 10$, 20, 30, 40, 50, we can see the disturbance amplitude-frequency characteristic curve, as shown in Figure 14:

From the above bode diagram, we can see that with the increase of w_c, w_0, T_a, the disturbance gain can be gradually reduced, observer bandwidth is gradually increasing, the improved LADRC controller's ability to track the total internal and external disturbances is gradually strengthened, that is, the system's anti-interference ability to external and internal is gradually strengthened.

C. IMMUNITY ANALYSIS OF IMPROVED LADRC COMBINED WITH WIND POWER SYSTEM

The stability of the bus voltage of the wind power inverter is mainly affected by the sudden change of the grid voltage and the disturbance of the load current. Next, the immunity

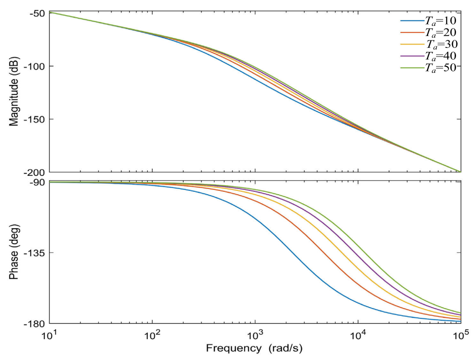

FIGURE 14. Frequency domain characteristic curve of disturbance term (Ta change).

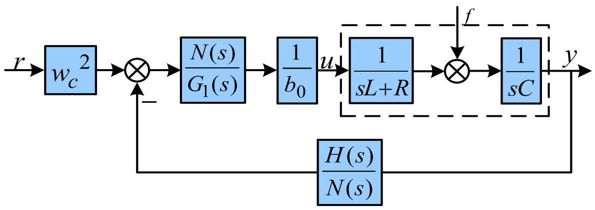

FIGURE 15. Improve the overall system structure of LADRC wind power grid connected inverter.

of bus voltage to load current under traditional LADRC and improved LADRC is compared. Figure 15 is the structure diagram of the wind power grid-connected inverter controlled by LADRC. From this, the transfer function of the DC bus voltage of the system can be obtained as:

$$\begin{aligned} U_{dc} &= \frac{N(s)w_c^2}{G_1(s)b_0(sL+R)sC+\mathrm{H}(s)}U_{ref} \\ &\quad+\frac{G_1(s)b_0(sL+R)}{G_1(s)b_0(sL+R)sC+\mathrm{H}(s)}f \\ &= G(s)+G_2(s) \end{aligned} \tag{38}$$

In the formula, U_{dc}, U_{ref}, f are system DC bus voltage, bus voltage reference value and total disturbance respectively; $G(s)$ is the transfer function from the bus voltage reference input to the actual output; $G_2(s)$ is the transfer function from the total disturbance to the actual output, that is, the anti-disturbance performance of the grid-connected inverter to maintain a stable bus voltage.

From the Bode diagram in Figure 16 above, it can be seen that the improved LADRC is significantly better than the traditional LADRC in the comparison of the anti-total interference ability in the middle and low-frequency bands; in the middle and low-frequency bands, the improved LADRC has a smaller disturbance gain, and its anti-interference ability is slightly better than that of the traditional LADRC; in the high-frequency range, the two curves roughly coincide.

D. STABILITY ANALYSIS OF IMPROVED LADRC

For the model proposed in this article, its stability is proved

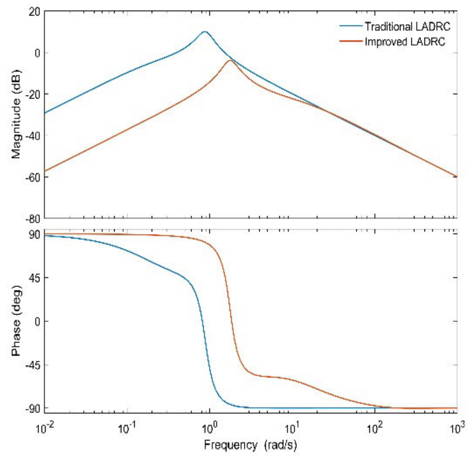

FIGURE 16. Improve the anti-interference amplitude and phase characteristic curve of LADRC and traditional LADRC.

According to RLESO

$$\begin{cases} \dot{z}_1 = z_2+\beta_1(z_1-\dot{y})+b_0u \\ \dot{z}_3 = \beta_2(z_1-\dot{y})+h(\dot{y},w) \\ z_3 = \dfrac{T_as+1}{aT_as+1}z_2 \\ \dot{y} = z_1 \end{cases} \tag{39}$$

where: $h(\dot{y},w)$ is the unknown total disturbance observed by RLESO.

Determine β according to equation (14). Let $\tilde{z}_i = z_i - \dot{y}_i$, $i = 1, 2, 3$, from (7) and (39), the improved RLESO estimation error formula is:

$$\begin{cases} \dot{\tilde{z}}_1 = \tilde{z}_3 - 2w_0\tilde{z}_1 \\ \dot{\tilde{z}}_3 = h(z,w) - h(\dot{y},w) - w_0^2\tilde{z}_1 \end{cases} \tag{40}$$

In the above formula, $h(y,w)$ is the actual value of the unknown total disturbance. To simplify the expression, take $\varepsilon_j = \frac{\tilde{z}_j}{w_0^{j-1}}$, $j = 1, 2, 3$, therefore, formula (40) can be reduced to:

$$\dot{\varepsilon} = w_0\begin{bmatrix} -2 & 1 \\ -1 & 0 \end{bmatrix}\begin{bmatrix} \varepsilon_1 \\ \varepsilon_1 \end{bmatrix}+\begin{bmatrix} 0 \\ 1 \end{bmatrix}\frac{h(z,w)-h(\dot{y},w)}{w_0} \tag{41}$$

Let

$$A_0 = \begin{bmatrix} -2 & 1 \\ -1 & 0 \end{bmatrix},\quad B_0 = \begin{bmatrix} 0 \\ 1 \end{bmatrix},\quad \varepsilon = \begin{bmatrix} \varepsilon_1 \\ \varepsilon_2 \end{bmatrix}.$$

From equation (14), it can be seen that the double pole in RLESO is at -w_0, and A_0 is stable on Hurwitz. Therefore, there is a positive definite hert matrix N, which can satisfy, $A_0^TN + NA_0 = -M$, and $N = \begin{bmatrix} 0.5 & -0.5 \\ -0.5 & 1.5 \end{bmatrix}$.

Define the lyapunov function $V(\varepsilon) = \varepsilon^TN\varepsilon$, then

$$\dot{V}(\varepsilon) = -w_0(\varepsilon_1^2+\varepsilon_2^2)+\frac{h(z,w)-h(\dot{y},w)}{w_0}(-\varepsilon_1+3\varepsilon_2) \tag{42}$$

Since $h(y,w)$ meets Lipschitz's conditions in the definition domain, so there is a constant c that makes

$|h(z,w)-h(\dot{y},w)| \leq c\,\|z-\dot{y}\|$, thus $\frac{h(z,w)-h(\dot{y},w)}{w_0}$ can satisfy:

$$\frac{h(z,w)-h(\dot{y},w)}{w_0}(-\varepsilon_1+3\varepsilon_2) \leq c(-\varepsilon_1+3\varepsilon_2)\frac{\|z-\dot{y}\|}{w_0} \tag{43}$$

By $-\varepsilon_1+3\varepsilon_2 = 2\varepsilon^T NB_0$, equation (43) can be transformed into

$$2\varepsilon^T NB_0\frac{h(z,w)-h(\dot{y},w)}{w_0} \leq 2c\varepsilon^T NB_0\frac{\|z-\dot{y}\|}{w_0} \tag{44}$$

When $w_0 \geq 1$, there are $\frac{\|z-\dot{y}\|}{w_0} = \frac{\|\dot{y}\|}{w_0} \leq \|\dot{y}\|$, at the same time because $\|NB_0c\|^2 - 2\,\|NB_0c\| + 1 \geq 0$, so there is:

$$2\varepsilon^T NB_0\frac{h(z,w)-h(\dot{y},w)}{w_0} \leq (\|NB_0c\|^2+1)\,\|\varepsilon\|^2 \tag{45}$$

When $w_0 > \|NB_0c\|^2 + 1$, $\dot{V}(\varepsilon) \leq 0$, according to the significance of Lyapunov's asymptotic stability, there are:

$$\lim_{x\to\infty} \tilde{z}_i(t) = 0, i = 1, 3 \tag{46}$$

From equation (24), we can see

$$u = \frac{K_p(r-z_1)-z_3}{b_0} \tag{47}$$

Let $e = r - z_1$ and get from equation (48)

$$u = \frac{K_p(e+\tilde{z}_1)-(z_3-\tilde{z}_3)}{b_0} \tag{48}$$

$$\dot{e} = \dot{r} - \dot{z} = -K_p(e+\tilde{z}_1) - \tilde{z}_3 + \dot{r} \tag{49}$$

The control signal of the maximum error is used to stimulate the controlled object, and the output signal can be quickly flowed out. Then the system becomes:

$$\dot{e} = -K_p(e+\tilde{z}_1) - \tilde{z}_3 \tag{50}$$

Write formula (50) in the form of state space as

$$\dot{e} = \begin{bmatrix} K_p \end{bmatrix} e(t) + \begin{bmatrix} K_p & -1 \end{bmatrix} \tilde{z}(t) \tag{51}$$

$-K_p$ can make the characteristic polynomial $s - K_p$ conform to routh criterion, so $\begin{bmatrix} -K_p \end{bmatrix}$ is stable on Hurwitz, and know, $\lim_{x\to\infty} \left\| \begin{bmatrix} K_p & -1 \end{bmatrix} \tilde{z}(t) \right\| = 0$, so $\lim_{x\to\infty} \|e(t)\| = 0$. According to Lyapulov's progressive theory, improving LADRC is progressively stable, which is equivalent to stability in the engineering sense.

VI. SIMULATION AND ANALYSIS

In order to verify the performance effect of the control system designed in this article, perform simulation research in MATLAB/Simulink environment, in the simulation research, this paper compares with the traditional LADRC method proposed in the literature [21], the parameter conditions in literature [21] are used for simulation verification.

TABLE 1. System parameters.

System parameters and units	Numerical value
Rated power/MW	1.5
Grid line voltage/V	690
Bus voltage/V	1070
Filter resistance/Ω	0.942
Filter inductor/uH	20
Capacitance/uF	240

TABLE 2. Controller parameters.

Controller parameters	Numerical value
Controller bandwidth/w_c	3200
Observer bandwidth/w_0	800
Controller gain/b_0	14000

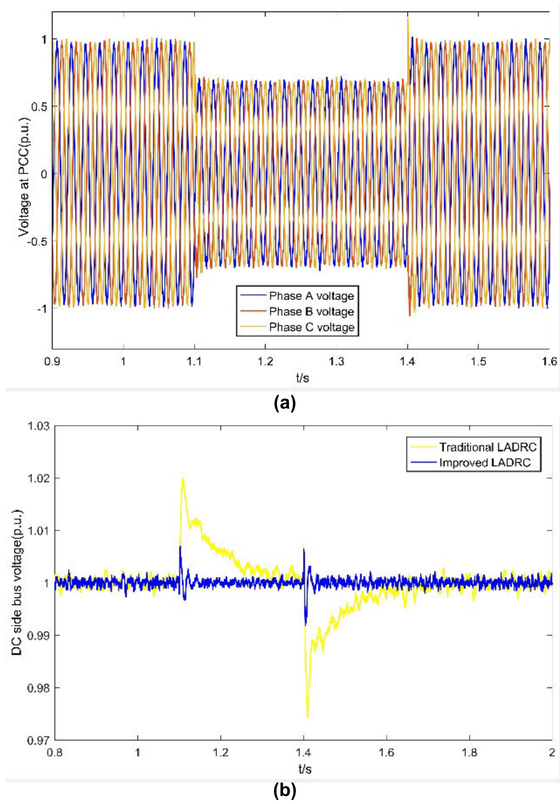

FIGURE 17. The voltage waveform of the busbar under the condition of symmetrical drop of 30% of the grid voltage; (a) Grid connected point voltage; (b) Symmetrical drop bus voltage.

A. SYMMETRICAL DROP FAILURE 30%

As can be seen from Figure 17, the DC bus voltage of the traditional LADRC control fluctuates from 0.973 pu to 1.021 pu during the low voltage crossing of 0.7 pu, the DC bus voltage fluctuation range under the improved LADRC control is 0.992pu∼1.006pu, and it can quickly reach a stable state of 1.0pu. In contrast, improved LADRC control has a better control effect on the stability of the DC bus voltage under

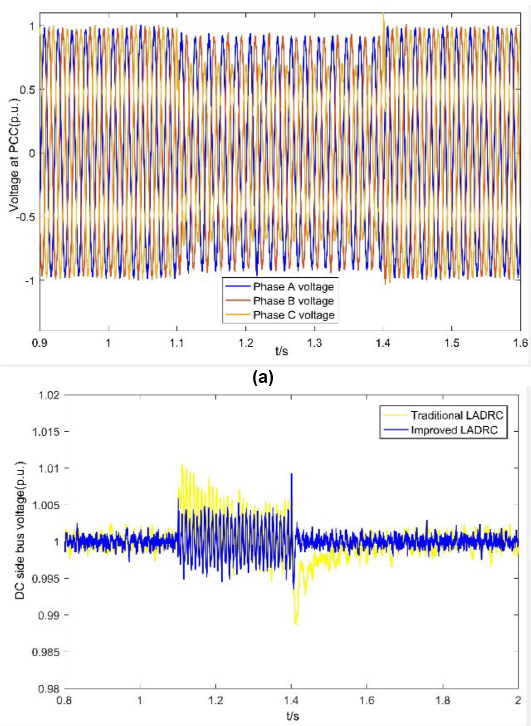

FIGURE 18. The voltage waveform of the busbar under the condition of 30% asymmetrical drop of the grid voltage; (a) Grid-connected point voltage; (b) Asymmetric drop bus voltage.

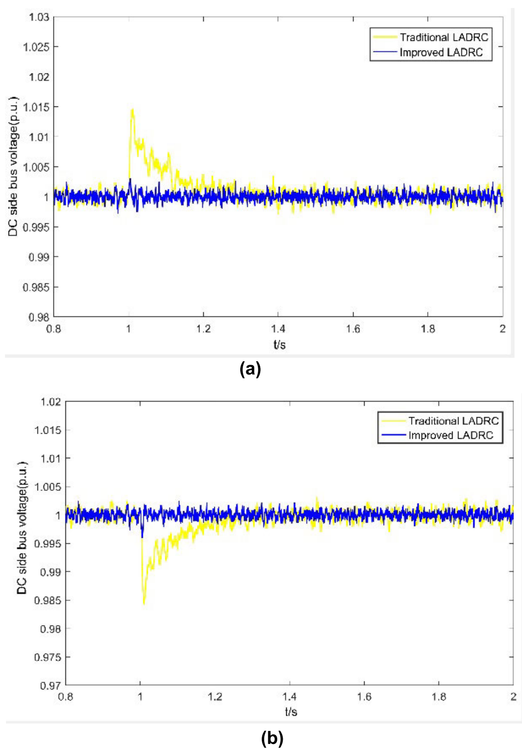

FIGURE 19. The bus voltage of the motor under load and unload conditions; (a) Motor load 30%; (b) Motor load reduction 30%.

disturbance conditions, it shows that the improved LADRC has better anti-interference performance, and is more suitable for actual system applications.

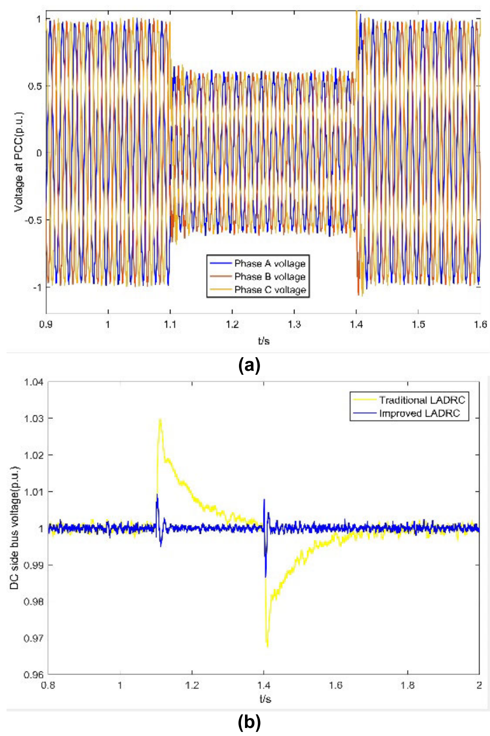

FIGURE 20. Bus voltage waveform under 40% symmetrical drop of grid voltage; (a) Grid-connected point voltage; (b) Symmetrical drop bus voltage.

B. ASYMMETRIC DROP FAILURE 30%

Figure 18 shows the grid voltage waveform and DC bus voltage waveform when the grid voltage is asymmetrically dropped. When it is set to 1.1s, the grid voltage asymmetrical drop failure occurs, the drop amplitude is 30%, and it returns to normal after 0.3s. It can be seen from Figure 18(b) that during a fault, the DC bus voltage of the improved LADRC control has a smaller fluctuation range, it shows that the improved LADRC's anti-interference performance is better than the traditional LADRC when the grid voltage is asymmetrical.

C. MOTOR LOADING AND UNLOADING 30%

Figure 19 shows the DC bus voltage waveform of grid-connected inverter when the motor is loaded and unloaded. Figure 19 (a) corresponds to the change of DC bus voltage when the motor is loaded with 30%, it can be seen that the overshoot of the DC bus voltage controlled by the traditional LADRC is 0.014pu, and the overshoot of the DC bus voltage controlled by the improved LADRC is 0.001pu. Figure 19 (b) corresponds to the change of the DC bus voltage when the motor load is reduced by 30%, it can be seen that the drop amplitude of the DC bus voltage controlled by the traditional LADRC is 0.016pu, and the drop amplitude of the DC bus voltage controlled by the improved LADRC is 0.001pu. It shows that the improved LADRC has better anti-interference performance than the traditional LADRC when the motor is loaded and unloaded.

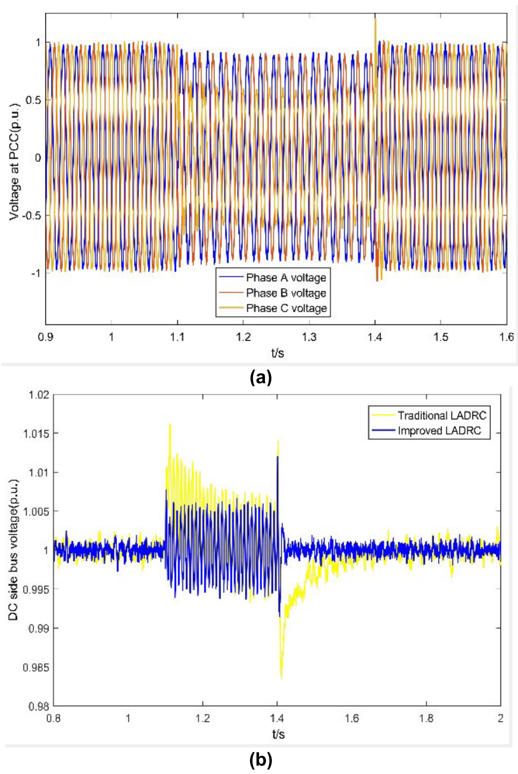

FIGURE 21. The voltage waveform of the busbar when the grid voltage drops 40% asymmetrically; (a) Grid-connected point voltage; (b) Asymmetric drop bus voltage.

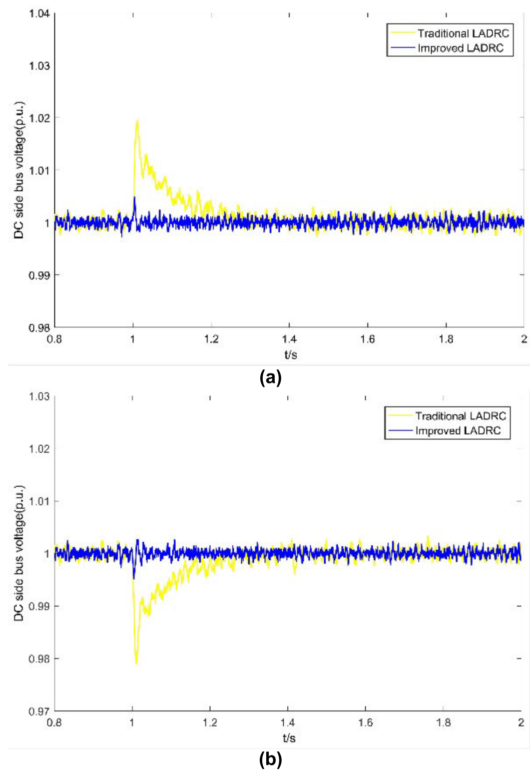

FIGURE 22. Bus voltage of motor under loading and unloading conditions; (a) Motor load 40%; (b) Motor load reduction by 40%.

D. SYMMETRICAL DROP FAILURE 40%

Figure 20 shows the grid voltage waveform and DC bus voltage waveform in case of grid voltage symmetrical drop fault. When the setting is 1.1s, asymmetrical drop of the grid voltage occurs, and the drop is 40%, and it returns to normal after 0.3s. As can be seen from Figure 20 (b), in case of fault, the overshoot of DC bus voltage controlled by traditional LADRC is about 0.029pu, and the overshoot of DC bus voltage controlled by improved LADRC is about 0.009pu; at the moment of fault recovery, the drop value of the DC bus voltage of the traditional LADRC control is about 0.035pu, and the drop value of the DC bus voltage of the improved LADRC control is about 0.015pu. And it can be seen from the figure that, compared with the traditional LADRC, the DC bus voltage controlled by the improved LADRC can enter the steady-state faster. Therefore, the improved LADRC has a stronger anti-interference ability when the grid voltage drops symmetrically.

E. ASYMMETRIC DROP FAILURE 40%

It can be seen from the 40% asymmetric drop in Figure 21 that the DC bus voltage fluctuation range of traditional LADRC control is 0.986pu∼1.016pu, and the DC bus voltage fluctuation range of improved LADRC control is 0.991pu∼1.014pu, and the improved LADRC can quickly To reach a steady state 1.0pu. From the above analysis, it can be known that improved LADRC control has a better control effect on the stability of the DC bus voltage under disturbance conditions.

F. MOTOR LOADING AND UNLOADING 40%

Figure 22 (a) corresponds to the change of the DC bus voltage when the motor is loaded with 40%, it can be seen that the overshoots of the DC bus voltage controlled by the traditional LADRC and the improved LADRC are 0.019 pu and 0.004 pu, respectively. Figure 22 (b) corresponds to the change of the DC bus voltage when the motor load is reduced by 40%, it can be seen that the drop amplitudes of the DC bus voltage of the traditional LADRC and the improved LADRC control are 0.021 pu and 0.01 pu, respectively. This phenomenon shows that the improved LADRC has better anti-interference performance than traditional LADRC when the motor is loaded and unloaded.

VII. CONCLUSION

In order to improve the stability of the DC side voltage of the direct-drive permanent magnet wind power grid-connected inverter, aiming at the shortcomings of traditional LADRC controllers, an improved LADRC voltage outer loop controller was designed, and a good control effect was achieved. The simulation results show that the designed voltage outer loop controller greatly improves the voltage response speed and reduces the fluctuation of DC voltage, The utilization rate of wind energy is improved, and the control effect is better than the traditional LADRC controller even when it is disturbed by the outside world, the simulation experiment also fully proved the effectiveness of the designed controller. The improved LADRC controller designed in this paper provides a new idea for the control of wind power grid-connected inverters and has a certain engineering application value.

REFERENCES

[1] S. Lei, *Research on Control Technology of Grid-Connected Inverter for 1.5 MW Wind Turbines*. Changchun, China: Changchun Univ. Technology, 2018.

[2] X. Zou, X. Du, and H. Tai, "Stability analysis for direct-drive permanent magnet synchronous generator based wind farm integration system considering wind speed," *IET Renew. Power Gener.*, vol. 14, no. 11, pp. 1894–1903, Aug. 2020.

[3] W. Xuan, *Research on Linear Active Disturbance Rejection Control Strategy of Three-level PWM Rectifier*. Xi'an, China: Xi'an Univ. Technology, 2018.

[4] L. Ping and W. Jiuhe, "Research on control strategy of Vienna rectifier based on passive and active disturbance rejection," *Power Grid Technol.*, pp. 1–12, Dec. 2021, doi: 10.13335/j.1000-3673.

[5] L. Xinrui, G. Chao, and W. Zhiliang, "DC bus voltage control of photovoltaic grid-connected inverter based on nonlinear disturbance observer," *Power Syst. Technol.*, vol. 44, no. 3, pp. 897–906, 2020.

[6] M. A. Hossain, H. R. Pota, A. M. O. Haruni, and M. J. Hossain, "DC-link voltage regulation of inverters to enhance microgrid stability during network contingencies," *Electr. Power Syst. Res.*, vol. 147, pp. 233–244, Jun. 2017.

[7] G. Jin, W. Lei, and L. Yi, "Research on grid-connected inverter of permanent magnet direct drive variable speed constant frequency wind power system," *Power Electron.*, vol. 51, no. 10, pp. 24–26, 2017.

[8] F. Diansen, *Research on the Control Technology of Wind Power Grid-Connected Inverter*. Zhuzhou, China: Hunan Univ. Technology, 2018.

[9] W. Guixin and J. Shenyi, "Research on control strategy based on three-phase voltage type PWM rectifier," *Elect. Drive*, vo. 49, no. 10, pp. 34–38, 2019.

[10] T. Meng, Z. Bowen, Z. Lawu, Y. Hongzhi, and L. Yan, "Research on sliding mode variable structure independent pitch control based on RBF neural network," *Power Syst. Protection Control*, vol. 47, no. 4, pp. 107–114, 2019.

[11] Z. Zubing, C. Lijuan, and G. Huixia, "Active disturbance rejection control strategy of voltage source PWM inverter," *J. Electrotechnics*, vol. 2, pp. 84–88, Jan. 2004.

[12] Y. Lin, Z. Jiang, M. Wenjie, and H. Zhonglong, "Voltage control of microgrid inverter based on improved second-order linear auto-disturbance rejection technology," *Automat. Electr. Power Syst.*, vol. 43, no. 4, pp. 146–153, 2019.

[13] W. Chunyang, Z. Shangqi, S. Hongwei, and L. Xuelian, "Linear active disturbance rejection control of airborne optoelectronic stabilized aiming platform," *Infr. Laser Eng.*, vol. 48, no. 12, pp. 248–254, 2019.

[14] M. Metwally Mahmoud, H. S. Salama, M. M. Aly, and A.-M.-M. Abdel-Rahim, "Design and implementation of FLC system for fault ride-through capability enhancement in PMSG-wind systems," *Wind Eng.*, vol. 45, no. 5, pp. 1361–1373, Oct. 2021.

[15] S. Jin, W. Zhao, J. Ji, and D. Xu, "Deadbeat direct power control for dual three-phase PMSG used in wind turbines," *IET Renew. Power Gener.*, vol. 15, no. 9, pp. 1976–1984, Jul. 2021.

[16] K. Vijayakumar, N. Kumaresan, and N. A. Gounden, "Operation and closed-loop control of wind-driven stand-alone doubly-fed induction generators using a single inverter-battery system," *IET Electr. Power Appl.*, vol. 6, no. 3, pp. 162–171, 2012.

[17] X. Zhou, M. Liu, Y. Ma, and S. Wen, "Improved linear active disturbance rejection controller control considering bus voltage filtering in permanent magnet synchronous generator," *IEEE Access*, vol. 8, pp. 19982–19996, 2020.

[18] L. Jie, Q. Xiaohui, W. Hui, and X. Yuanqing, "Active disturbance rejection control: Summary and prospects of research results," *Control Theory Appl.*, vol. 34, no. 3, pp. 281–295, 2017.

[19] Z. Gao, "Scaling and bandwidth-parameterization based controller tuning," in *Proc. Amer. Control Conf.*, Jun. 2003, pp. 4989–4996.

[20] Y. Dong, M. Xiaojun, Z. QingHan, and Q. Xiaobo, "Research on frequency band characteristics and parameter configuration of linear ADRC for second-order systems," *Control Theory Appl.*, vol. 30, no. 12, pp. 1630–1640, 2013.

[21] Y. Dong, M. Xiaojun, Z. Qinghan, and Q. Xiaobo, "Study on frequency band characteristics and parameter configuration of linear active disturbance rejection controller for second-order system," *Control Theory Appl.*, vol. 30, no. 12, pp. 1630–1640, 2013.

CHANGSHENG YUAN received the M.S. degree from the School of Electrical Engineering, Tianjin University of Technology, China, in 2021. He is currently working with The 16th Research Institute of China Electronics Technology Group Corporation. His research interests include active disturbance rejection control technology and grid inverter.

XUESONG ZHOU received the B.S. degree from the South China University of Technology, Guangzhou, China, in 1984, and the M.S. and Ph.D. degrees from Tsinghua University, Beijing, China, in 1990 and 1993, respectively. From 1993 to 2002, he worked with the School of Electrical and Automation Engineering, Qingdao University, as the Deputy Dean and the Director of the Shandong Provincial Key Laboratory of Power Electronics Engineering. In 1997, he was promoted to a Full Professor at Qingdao University. Since 2002, he has been working with the School of Electrical and Electronic Engineering, Tianjin University of Technology, Tianjin, China. His research interests include power system analysis and automation, smart grid, and the field of new energy utilization.

YOUJIE MA received the B.S., M.S., and Ph.D. degrees from Tsinghua University, Beijing, China, in 1987, 1990, and 1993, respectively. From 1993 to 2002, she worked with the School of Electrical and Automation Engineering, Qingdao University, where she was promoted to a Full Professor, in 1998. Since 2002, she has been working as a Distinguished Professor with the School of Electrical and Electronic Engineering, Tianjin University of Technology, Tianjin, China. Her research interests include power system analysis and automation and smart grid.